Optimization of Extreme Ultraviolet Emission from Laser-Produced Tin Plasmas Based on Radiation Hydrodynamics Simulations

Atsushi SUNAHARA, Katsunobu NISHIHARA[1)] and Akira SASAKI[2)]

Institute for Laser Technology, 2-6 Yamadaoka Suita Osaka 565-0871, Japan

[1)] *Institute of Laser Engineering, Osaka University, 2-6 Yamadaoka Suita Osaka 565-0871, Japan*

[2)] *Advanced Photon Research Institute of Japan Atomic Energy Agency, 8-1 Umemidai Kizugawa Kyoto 619-0215, Japan*

(Received 14 April 2008 / Accepted 6 June 2008)

We investigated the plasma conditions for obtaining highly efficient extreme ultraviolet light from laser-produced tin plasmas for lithography of next generation semiconductors. Based on accurate atomic data tables calculated using the detailed configuration accounting code, we conducted 1-D radiation hydrodynamic simulations to calculate the dynamics of tin plasma and its emission of extreme ultraviolet light. We included the photo-excitation effect in the radiation transport. Our simulation reproduced experimental observations successfully. Using our verified code, we found that a CO_2 laser can be useful in obtaining higher conversion efficiencies up to 4%.

Keywords: EUV, lithography, radiation hydrodynamics, conversion efficiency, laser-produced tin plasma

DOI: 10.1585/pfr.3.043

1. Simulation Model

Extreme ultraviolet (EUV) emission from laser-produced plasmas can be used as the light source used in lithography of next generation semiconductors [1]. For industrial applications, we must understand the physical process of EUV emission from laser-produced plasmas, and optimize various parameters in the laser and target conditions. Tin is considered to be the most attractive for EUV emission as its plasma emits 13.5 nm EUV with a 2% bandwidth [2]. To simulate EUV emission from laser-produced tin plasmas, we developed a 1-D Lagrangian radiation hydrodynamic code, "Star-1D." In our code, we used the one-fluid and two-temperature model, i.e., a single momentum equation for fluid and an energy equation for each of ion and electron. Thus, the following four equations are solved:

$$\frac{\mathrm{D}\rho}{\mathrm{D}t} = -\rho\nabla\cdot\vec{v}, \tag{1}$$

$$\rho\frac{\mathrm{D}v}{\mathrm{D}t} = -\nabla(p+q), \tag{2}$$

$$\rho c_{\mathrm{vi}}\frac{\mathrm{D}T_{\mathrm{i}}}{\mathrm{D}t} = -(p_{\mathrm{THi}}+q)\nabla\cdot\vec{v} + \nabla\cdot(\kappa_{\mathrm{i}}\nabla T_{\mathrm{i}}) + \alpha(T_{\mathrm{e}}-T_{\mathrm{i}}), \tag{3}$$

$$\rho c_{\mathrm{ve}}\frac{\mathrm{D}T_{\mathrm{e}}}{\mathrm{D}t} = -p_{\mathrm{THe}}\nabla\cdot\vec{v} + \nabla\cdot(\kappa_{\mathrm{e}}\nabla T_{\mathrm{e}}) - \alpha(T_{\mathrm{e}}-T_{\mathrm{i}}) + Q_{\mathrm{L}} + Q_{\mathrm{r}}. \tag{4}$$

Here $\vec{v}$, ρ, p_{i}, p_{e} (e = electron and i=ion) and q are, the velocity, mass density, ion pressure, electron pressure and the artificial viscosity, respectively. The total pressure p is defined by $p = p_{\mathrm{i}} + p_{\mathrm{e}}$. In Eqs. (3) and (4), p_{THi} and p_{THe} are defined as $p_{\mathrm{THi}} = T_{\mathrm{i}}(\partial p_{\mathrm{i}}/\partial T_{\mathrm{i}})$ and $p_{\mathrm{THe}} = T_{\mathrm{i}}(\partial p_{\mathrm{e}}/\partial T_{\mathrm{e}})$, respectively. c_{vi} and T_{i} represent the specific ion heat and ion temperature, and c_{ve} and T_{e} represent the specific electron heat and electron temperature, respectively. κ_{i} and κ_{e} are the ion [3] and electron conductivities [4], respectively. $\alpha(T_{\mathrm{e}} - T_{\mathrm{i}})$ in Eqs. (3) and (4) is the electron-ion temperature relaxation term. Here α is determined by the Spizer relaxation time [5]. In Eqs. (3) and (4), the ion and electron heat conductions are calculated simultaneously and we applied the flux-limited Spitzer-Harm model [6] with a flux-limiter of 0.1. The source term Q_{L} in Eq. (4) is the heating term due to the laser heating term for electrons. For the laser absorption process, we assumed the inverse-bremsstrahlung [7]. The laser energy deposited between the vacuum plasma boundary and the critical surface is calculated by ray-tracing with 100 rays. The laser absorption coefficient is given by the energy deposition rate due to the inverse-bremsstrahlung process. The energy damping rate due to inverse-bremsstrahlung ν_{abs} is given by $\nu_{\mathrm{abs}} = 1.195\times10^{-3}Z^*\ln\Lambda f\widetilde{n}^2/\lambda_{\mu\mathrm{m}}^2(k_{\mathrm{B}}T_{\mathrm{e}})^{3/2}$, where Z^* is the effective charge defined as $Z^* = \langle z^2\rangle/\langle z\rangle$, $\langle\ \rangle$ indicates averaging over the ion species. $\ln\Lambda$ is the Coulomb logarithm [8]. $\widetilde{n}$ is the normalized electron density, which is defined as $\widetilde{n} = n_{\mathrm{e}}/n_{\mathrm{critical}}$. n_{e} and n_{critical} are the electron density and the critical density of laser, respectively. k_{B} is the Boltzmann constant. $\lambda_{\mu\mathrm{m}}$ is the laser wavelength in μm unit, respectively. f is the reduction factor of the

author's e-mail: suna@ile.osaka-u.ac.jp

laser absorption due to the Langdon effect [9], which is important for long-wavelength laser irradiation.The laser energy deposition for each calculation mesh is calculated by $P_{\rm exp}(-\nu_{\rm abs}\Delta t)$, where P is the local laser ray power, and Δt is the time required for the laser ray to pass through each mesh size at its group velocity $v_{\rm g} = c(1-\widetilde{n})^{1/2}$. Here c is the speed of light. In Eqs. (2) to (4), the variables p_s, c_{vs}, $p_{\rm ths}$, $\langle Z\rangle$ and $\langle Z^2\rangle$ are the functions of $n_{\rm i}$ and T_s. Here, s represents an electron or ion, which is obtained from the tabulated equation of state based on the averaged atomic model. For the equation of state for ions, we adopt the Cowan model [10], and for electrons at the low-temperature and high-density limit, we use the QEOS model [10]. The source term $Q_{\rm r}$ in Eq. (4) is the heating term due to radiations. For evaluating the radiation transport, we applied the multi-group diffusion approximation model [11] using the flux-limiter, as given below.

$$\rho\frac{\mathrm{D}}{\mathrm{D}t}\left(\frac{E^\nu}{\rho}\right) - \Omega\cdot(D^\nu\nabla E^\nu) = 4\pi\eta^\nu - c\chi^\nu E^\nu \qquad (5)$$

where, D^ν is the diffusion coefficient defined by $D^\nu = c/(3\chi^\nu + c|\nabla E^\nu|/E^\nu)$. E^ν is the photon energy density at the energy $h\nu$. Ω is the x-ray propagation direction, which is set to be the spatial coordinate in this paper, and c is the speed of light. For solving Eq. (5) numerically, the photon energy ranging from 0 to 1.5 keV was divided into 1500 bins. η^ν and χ^ν are the emissivity and the attenuation coefficient (density × opacity). They were obtained from the Hullac code, where atomic energy levels are calculated with the detailed configuration accounting, and the electron population at each atomic level is calculated by solving rate equations among the many atomic energy levels [12]. Energy levels calculated using Hullac were adjusted to those of experimental observation by charge exchange spectroscopy [13]. The conventional method is used to calculate their emissivity $\eta^\nu_{\rm CRE}$ and opacity $\kappa^\nu_{\rm CRE}$ based on the Collisional Radiative Equilibrium (CRE) model [14]. However, the conventional CRE model has no photo-excitation or photo-ionization, because it is assumed to be an optically thin plasma, where the optical thickness which is defined as $\int_x^\infty \chi^\nu(x')\mathrm{d}x'$ should be less than 1. For tin plasma $\chi^{\rm EUV}$ can be large due to its large opacity in EUV region, and may result in a EUV optical thickness $\int_x^\infty \chi^{\rm EUV}(x')\mathrm{d}x'$ of more than 1, in which the assumption of an optically thin plasma is not valid, and the re-absorption of x-ray radiation is not negligible. Such a condition should be regarded as the optically thick. In the optically thick limit, where $\int_x^\infty \chi^\nu(x')\mathrm{d}x' \gg 1$, the radiation field and electrons in the material are in the local thermal equilibrium (LTE), and the radiation field becomes Planck radiation given by the local electron temperature $T_{\rm e}(x)$ as the results of successive photo-excitation (absorption) and photo-emission in the material. In such a condition, we can calculate the electron population of each energy levels, which is consistent with the Planck radiation field, and also the emissivity $\eta^\nu_{\rm LTE}$ and opacity $\kappa^\nu_{\rm LTE}$ based on the LTE assumption can be evaluated. We use the Novikov method in order to include the photo-excitation in our simulation [15]. In this model, the emissvity and opacity are obtained by the interpolation of that with CRE and LTE as follows,

$$\eta^\nu = \xi_\nu\eta^\nu_{\rm LTE} + (1-\xi_\nu)\eta^\nu_{\rm CRE}, \qquad (6)$$

$$\kappa^\nu = \xi_\nu\kappa^\nu_{\rm LTE} + (1-\xi_\nu)\kappa^\nu_{\rm CRE}. \qquad (7)$$

Here, $\xi_\nu = E^\nu(x,t)/U^\nu(T_{\rm e}(x),t)$ and E^ν is the calculated radiation energy density with energy $h\nu$ and U^ν is the Planck radiation energy density given by the local temperature $T_{\rm e}$. x is the space and t is the time. In this model, in the optically thin limit ($\xi_\nu \ll 1$) CRE emissivity and opacity are used. In the optically thick limit ($\xi_\nu \gg 1$), LTE emissivity and opacity are used. In the intermediate region ($0 < \xi^\nu < 1$), emissivity and opacity are calculated according the degree of planckian ξ_ν for each photon energy $h\nu$. In our calculation, we use the emissivity $\eta_{\rm LTE}(n_{\rm e}, T^*_{\rm e})$ and opacity $\xi_{\rm LTE}(n_{\rm e}, T^*_{\rm e})$ so as to give $\langle Z\rangle_{\rm LTE}(n_{\rm e}, T^*_{\rm e}) = \langle Z\rangle_{\rm LTE}(n_{\rm e}, T_{\rm e}(x'))$. Using $T^*_{\rm e}$ instead of $T_{\rm e}(x')$, we can consider the photo-excitaiton only, but not photo-ionization. The Novikov model requires that the electron population with LTE and CRE be slightly different due to the photon process. Including photo-ionization may make the population very different for LTE and CRE, and the interpolation scheme becomes invalid.

In Fig. 1, we show a typical profile of the ion density $n_{\rm i}$, electron temperature $T_{\rm e}$, ionization degree $\langle Z\rangle$, $\xi_{\rm EUV}$ defined as the $\xi_{\rm EUV} = \int_{13.4{\rm nm}}^{13.6{\rm nm}} E^\nu\mathrm{d}\nu / \int_{13.4{\rm nm}}^{13.6{\rm nm}} U^\nu\mathrm{d}\nu$, EUV flux, and EUV source S^* defined as $S^* = 4\pi\eta^{\rm EUV} - c\chi^{\rm EUV}E^{\rm EUV}$ at the laser peak timing based on the collisional radiative equilibrium (CRE) model, and CRE model with the photo-excitation, respectively. A 1.06 μm wavelength laser is irradiated on the tin plate with a 2.2 ns Gaussian pulse duration. The laser intensity is 1.0×10^{11} W/cm^2. We see that $\xi_{\rm EUV}$ are located between 0 and 1 around the EUV emission region. Compared with radiation transport based on the CRE model, the Novikov model (represented by w/ photo-excitation (PE)) gives a higher EUV source S^* and EUV flux, due to the increase in the excited electron population and decrease of opacity.

2. Benchmark Test

Figure 2 shows a comparison of calculated EUV conversion efficiencies (CE) from the incident laser energy to EUV, with a conventional CRE model (CRE), Novikov model (CRE with photo-excitation (PE)), and the experimental observations [16]. In the experiments, a 1.06 wavelength 2.2 ns duration pulse (FWHM) was irradiated on the tin plate. The laser spot diameter is 660 μm for a laser intensity less than 2×10^{11} W/cm^2, and 270 μm for a laser intensity more than 2×10^{11} W/cm^2. Sound velocity has an order of 10^6 cm/s for the tin EUV plasma. In this experimental condition, the plasma expansion length is estimated to be less than 150 μm, and is less than the laser

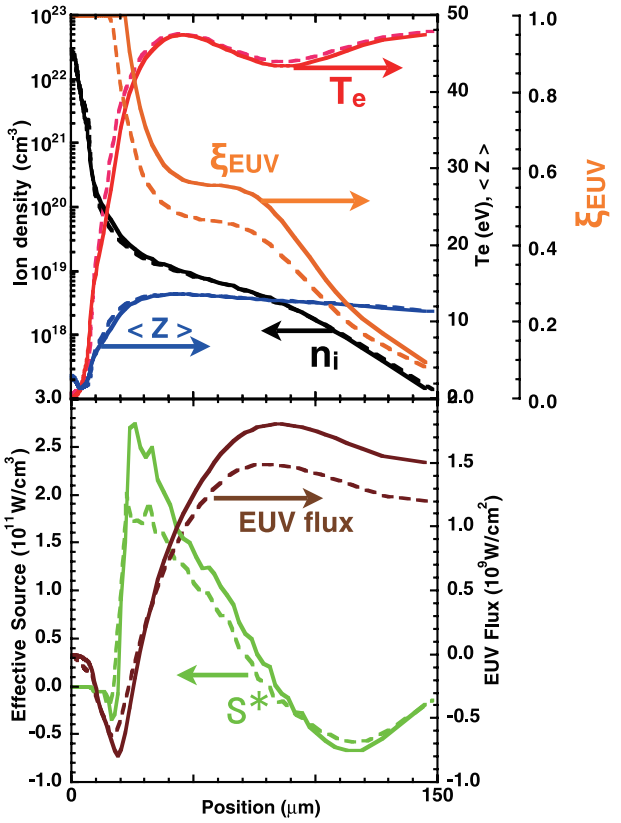

Fig. 1 Spatial profile of n_i, T_e, $\langle Z \rangle$, ξ_{EUV}, EUV flux, EUV source for the CRE model (solid), and CRE with photo-excitation (dotted), respectively at the laser peak timing.

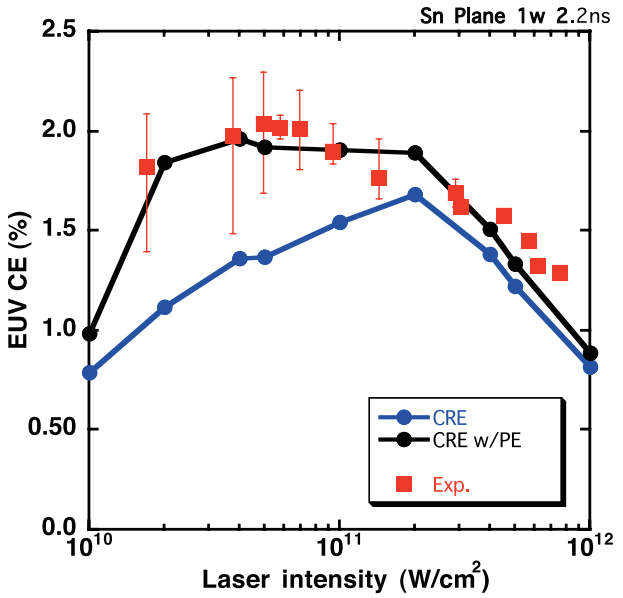

Fig. 2 Conversion efficiency (CE) from laser to EUV. A 2.2 ns duration pulse with a 1.06 μm wavelength laser is irradiated on the tin plate. The solid black line is the CRE with photo-excitation (PE), the solid blue line is the CRE, and the red points are the experimental data.

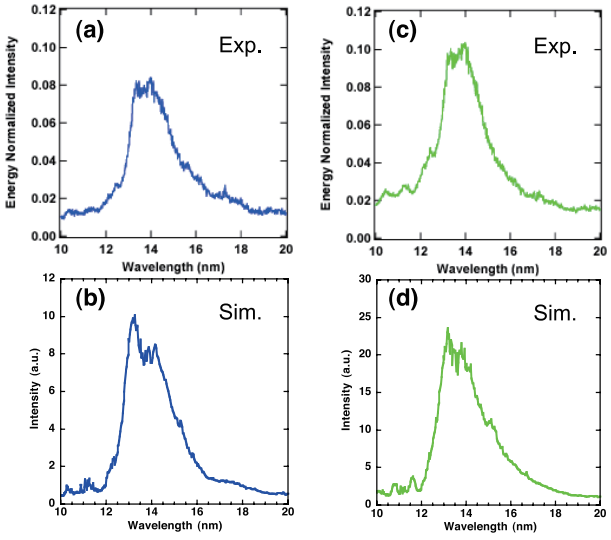

Fig. 3 Comparison of EUV spectra. (a) Experiment with 4×10^{10} W/cm^2. (b) Calculated with 4×10^{10} W/cm^2. (c) Experiment with 1×10^{11} W/cm^2. (d) Calculated with 1×10^{11} W/cm^2.

spot diameter. The estimation of scale length is consistent with Fig. 1, where we see the density scale length of EUV emission region is about 50 μm.(1/e definition). Thus, one dimensionality is confirmed in this experiment. In Fig. 2, we see that EUV CE calculated with CRE and PE is in good agreement with the experimental results. EUV CE with CRE, however, shows a different trend and a large discrepancy can be seen especially for the low laser intensities.

EUV spectra are shown in Fig. 3. We show two different conditions of the laser intensity of 4×10^{10} W/cm^2 in Figs. 3 (a) and (b), and the laser intensity of 1×10^{11} W/cm^2 in Figs. 3 (c) and (d). Figures 3 (a) and (c) are experimental spectra, and Figs. 3 (b) and (d) are calculations, The calculated spectra are in good agreement with the experimental results for both conditions. By comparison, around 13.5 nm, we see a tiny discrepancy of absorption dips in Fig. 3. The calculated spectra shown in Figs. 3 (b) and (d) show shallow absorption dips; however, they do not appear in the experimental results. Our calculations are entirely one dimensional, however, a real plasma includes the 3-D expansion. We think that these differences in spectra are due to the non-1D expansion effect in the real plasma and resulted in decrease of the EUV optical depth. However, differences are not so large, and we can regard this condition as the 1-D plasma. From above comparison, we verified that our radiation hydrodynamic simulation can reproduce the experimental EUV CE and its spectrum for a one-dimensional tin plasma quantitatively with a high accuracy .

3. Optimization of Laser Wavelength

Next, we optimize the tin plasma condition to obtain higher EUV CE by using our radiation hydrodynamic sim-

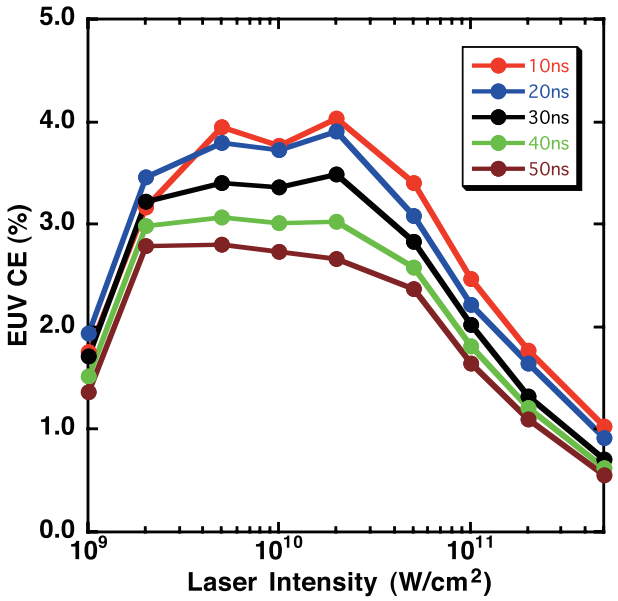

Fig. 4 EUV CE with CO_2 irradiation on tin plate. Various pulse durations and laser intensities are calculated.

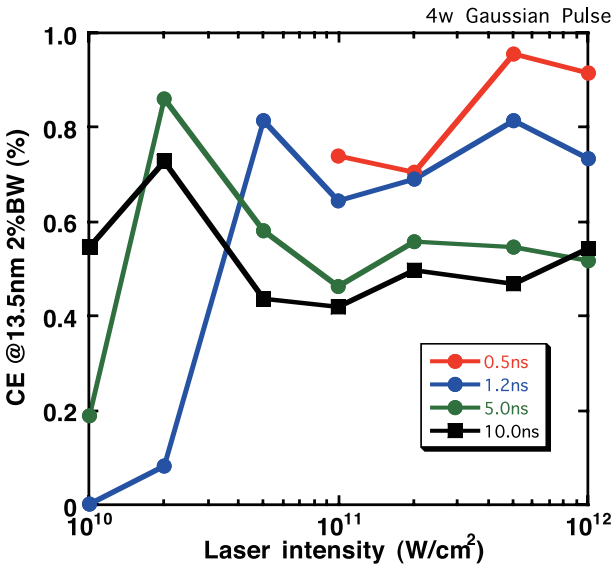

Fig. 5 EUV CE with a 0.25 μm wavelength laser irradiating a tin plate. Various pulse durations and laser intensities are calculated.

ulation code. We show the calculated EUV CE for the 10.6 μm wavelength (CO_2) laser with various laser intensities in Fig. 4. We see that a high EUV CE up to 4% can be obtained around a laser intensity of 1×10^{10} W/cm^2. This optimum laser intensity is one order lower than that for the 1.06 μm laser wavelength laser. As the laser pulse duration increases, EUV CE gradually decreases due to the larger EUV optical depth. In Fig. 4, a 10 ns duration pulse gives a maximum EUV CE of 4%. Next, we show the calculated EUV CE for the 0.25 μm wavelength laser with various laser intensities in Fig. 5. Compared with the CO_2 case in Fig. 4, the shorter 0.26 μm wavelength laser gives a lower EUV CE. As the laser pulse duration increases beyond 0.5 ns, the EUV CE decreases to less than 1%. Also, the optimum laser intensity for a maximum EUV CE is around 10^{12} W/cm^2, which is one order higher than that with the 1.06 μm wavelength laser. Comparing Figs. 2, 4, and 5, we can conclude that a longer wavelength laser provides higher EUV conversion efficiency for a one-dimensional plane plasma of tin. This result is consistent with the analysis by the power balance model developed by Nishihara *et al.*[17]. In Fig. 6, we show a comparison of EUV spectra for 10.6 μm wavelength, CO_2 laser and 1.06 μm laser at a laser intensity of 3×10^{10} W/cm^2 and 10 ns duration pulse. Obviously, the spectrum for the CO_2 laser is narrower than for the 1.06 μm laser. In real industrial applications, 10.6 μm wavelength CO_2 lasers are widely used. From this analysis, we can conclude that a CO_2 laser is useful for obtaining higher EUV CE from a laser-produced tin plasma in a one-dimension plane geometry for exteme Ultraviolet lithography.

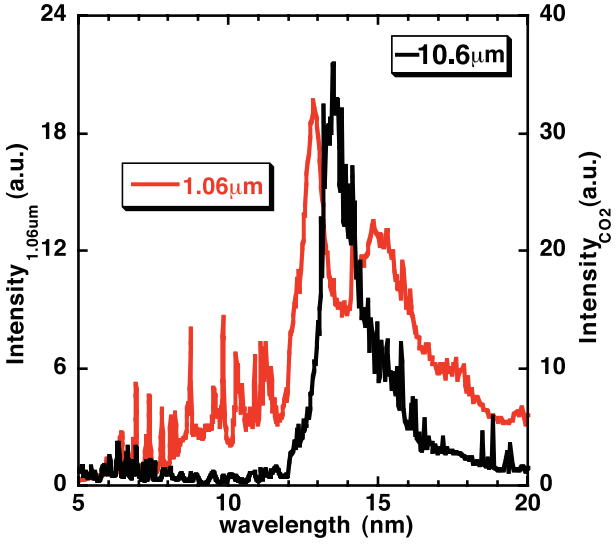

Fig. 6 Comparison of calculated spectra with 1.06 μm wavelength laser and with 10.6 μm wavelength CO_2 laser

4. Summary

In summary, we developed a 1-D radiation hydrodynamic code that included the photo-excitation effect. Photo-excitation is not negligible in a laser-produced tin plasma emitting EUV. The inclusion of photo-excitation gives a higher EUV CE compared to that with the conventional CRE model without PE, and reproduces the experimental observations for a laser-produced one-dimensional plasma of tin. Our simulation results showed that longer wavelength CO_2 laser yields higher EUV CE. With CO_2 laser, we estimated the EUV CE to be as high as 4% at a laser intensity of 1×10^{10} W/cm^2. Our analysis is limited

to be one-dimensional plane plasma of tin. In real applications, the 3-D expansion effect due to the finite laser spot diameter should be addressed. In the future, this analysis will be done by multi-dimensional simulation.

Part of this work has been conducted under the auspices of Leading Project promoted by MEXT.

[1] V. Bakshi editor *EUV Sources for Lithography* (SPIE Press., 2005).
[2] R.C. Spitzer, R.L. Kauffman, T. Orzechowski, D. Phillion and C. Cerjan, J. Vac. Sci. Technol B **11**, 2986 (1993); R.C. Spitzer *et al*., J. Appl. Phys. **79**, 2251 (1996).
[3] S.I. Braginskii, Reviews of Plasma Physics, **1**, Consultants Bureau 205(1965). **1**, 265 (1958).
[4] L. Spitzer Jr. and R. Harm, Phys. Rev. **89**, 977 (1953).
[5] L. Spitzer Jr., *Physics of Fully Ionized Gases* (John Wiley & Sons Inc., 1962) p.115.
[6] R.C. Malone, R.L. McCrory and R.L. Morse, Phys. Rev. Lett. **34**, 721 (1975).
[7] W.L. Kruer, *The physics of Laser Plasma Interactions* (Addison-Wesley Pub., 1988) p.48.
[8] S. Skupsky, Phys. Rev. A **36**, 5701 (1987).
[9] A.B. Langdon, Phys. Rev. Lett. **44**, 575(1980).
[10] R.M. More, K.H. Warren, D.A. Young and G.B. Zimmerman, Phys Fluids **31**, 3059 (1988).
[11] R.C. Malone, R.L. McCrory and R.L. Morse, Phys. Rev. Lett. **34**, 721 (1975).
[12] A. Sasaki, J. Plasma Fusion Res. **79**, 315 (2003) ; A. Sasaki, K. Nishihara, A. Sunahara, T. Nishikawa, F. Koike, K. Kagawa and H. Tanuma Proc. SPIE **6151**, 61513W (2006) ; A. Sasaki *et al*., Appl. Phys. Lett. **85**, 5857 (2004).
[13] H. Tanuma and A. Sasaki, J. Plasma Fusion Res. **83**, 679 (2007) ; H. Ohashi, H. Tanuma, S. Fujioka, H. Nishimura, A. Sasaki and K. Nishihara, J. Phys. Conf. **58**, 235 (2007) ; H. Tanuma, H. Ohashi, S. Fujioka, H. Nishimura, A. Sasaki and K. Nishihara, J. Phys. Conf. **58**, 231 (2007).
[14] D. Zaltzmann, *Atomic Physics in Hot Plasmas* (New York, Oxford University Press. 1998) Chap.4.
[15] A.F. Nikiforov, V.G. Novikov, V.B. Uvarov and A. Iacob, *Quantum-Statistical Models of Hot Dense Matter: Methods for Computation and Equation of State* (Progress in Mathematical Physics, Birkhauser, 2005).
[16] T. Ando *et al*., Appl. Phys. Lett. **89**, 151501 (2006).
[17] K. Nishihara, A. Sasaki, A. Sunahara and T. Nishikawa, "Conversion Efficiency of LPP source" (Chap. 11) of *EUV Sources for Lithography*, (SPIE press, edited by Vivek Bakshi, PM149, 2006) 339-371.